nuclear fusion
IAEA

PAPER • OPEN ACCESS

Infernal instabilities in negative-triangularity plasmas with negative central shear

To cite this article: X.M. Zhang *et al* 2025 *Nucl. Fusion* **65** 026066

OPEN ACCESS
IOP Publishing | International Atomic Energy Agency
Nuclear Fusion
Nucl. Fusion **65** (2025) 026066 (12pp)
https://doi.org/10.1088/1741-4326/adac78

Infernal instabilities in negative-triangularity plasmas with negative central shear

X.M. Zhang[1,2], L. Li[1,2,*], Y.Q. Liu[3], Z.Y. Dong[1,2], J.W. Li[1,2], Y. Liang[1,2,4] and F.C. Zhong[1,2]

[1] College of Science, Donghua University, Shanghai 201620, China
[2] Member of Magnetic Confinement Fusion Research Centre, Ministry of Education, Shanghai 201620, China
[3] General Atomics, PO Box 85608, San Diego, CA 92186-5608, United States of America
[4] Forschungszentrum Julich GmbH, Association EURATOM-FZ Jülich, Institut für Energieforschung—Plasmaphysik, Trilateral Euregio Cluster, D-52425 Jülich, Germany

E-mail: lili8068@dhu.edu.cn

Received 8 March 2024, revised 11 January 2025
Accepted for publication 21 January 2025
Published 31 January 2025

Abstract

A systematic numerical investigation is carried out to understand magnetohydrodynamic stability of the ideal infernal-kink instability in tokamak plasmas with both negative triangularity (neg-D) shaping and negative central shear for the equilibrium safety factor profile. The latter is motivated by the desire to form the internal transport barrier in the neg-D configuration, which is known to have difficulty in forming the edge transport barrier. The infernal-kink mode is generally found to be more unstable in neg-D plasmas as compared to their positive D-shaped (pos-D) counterpart. This is mainly due to less favorable (or even unfavorable) average magnetic curvature near the radial location of the minimum safety factor ($q_{\min}$) as compared to the pos-D configuration. The larger Shafranov shift associated with the neg-D shape helps the mode stabilization but is not sufficient to overcome the destabilizing effect due to bad curvature. Strong poloidal mode coupling due to plasma shaping (toroidicity, elongation, triangularity, etc.) helps explain the slight shift with respect to that predicted by the analytic theory of the peak location of the computed mode growth versus $q_{\min}$.

Keywords: plasma triangularity, infernal-kink instability, negative central shear

(Some figures may appear in colour only in the online journal)

* Author to whom any correspondence should be addressed.

1. Introduction

The presence of the edge transport barrier (ETB) in tokamaks can enhance the performance in the core plasma and increase the non-inductive bootstrap current, while simultaneously reducing the external heating power requirements, thereby improving the economy of fusion energy [1–3]. The dominant choice for most present tokamak devices is therefore to operate in H-mode, as it allows for good confinement performance and higher operating parameters [4].

However, the operation of H-mode still presents a multitude of challenges [5–7], including: (i) the strong interaction between the plasma and plasma facing components (PFCs) ascribed to the presence of the ETB; (ii) the inherent conflict between the damage limit of PFCs and the threshold for the transition between L-mode and H-mode; (iii) intricacies in controlling detached regimes; and (iv) triggering of the so-called type-I ELMs that lead to the exhaust issues.

Recent experimental results obtained from DIII-D [8–10] and TCV [11–15], featuring negative triangularity shapes (neg-D), present a promising approach to address the aforementioned challenges associated with ETB in plasma [11, 16–19]. The absence of a strong ETB in neg-D plasmas allows access to an ELM-free regime but still with good confinement [20, 21]. However, further careful investigation is required to comprehend the MHD instability in these neg-D configuration plasmas.

The negative central shear (NCS) is often associated with, and facilitates the formation of, the internal transport barrier (ITB), which in turn offers one promising scenario for the advanced tokamak (AT) concept based on conventional pos-D shape [22–25]. A NCS scenario with ITB may also improve confinement in neg-D plasmas. Indeed, as plasma triangularity vanishes toward the magnetic axis, the NCS configuration may be achievable in the plasma core of neg-D discharges where shaping differences between pos-D and neg-D plasmas are minimal [26, 27].

However, an equilibrium with NCS is known to be prone to the infernal, sometimes also referred to as the quasi-interchange, instability as has been frequently studied for plasmas with pos-D shapes [28–33]. This type of instability often occurs when the minimum q-value ($q_{\min}$) is close to a rational number, and when there is a sufficient pressure drive at the radial location of $q_{\min}$ [19, 28, 34]. Onset of an infernal mode may complicate plasma operation during the current ramp-up phase (as $q_{\min}$ evolves), or produce the so-called long-lived mode (LLM) as observed in experiments [35, 36]. Furthermore, as will be reported in this work, this instability can also couple to an external kink mode in plasmas with relatively high (global) pressure, resulting in what we refer to here as the infernal-kink mode, with the associated eigenmode sharing characteristics of both the infernal and kink instabilities. The main purpose of the present work is to provide a systematic investigation of the infernal-kink instability in plasmas with NCS and with neg-D shape. For comparison, we will also consider pos-D plasmas with otherwise similar radial profiles for the equilibrium quantities, such as the safety factor and the plasma pressure.

The work is organized as follows. Section 2 briefly introduces computational model and a series of equilibria with varying plasma boundary shape. In section 3, a systematic study of the effect of the triangularity on infernal/infernal-kink instabilities is presented, considering various q-profiles and wall conditions. Finally, section 4 summarizes the work.

2. Modeling tool and equilibria

2.1. Modeling tool

In this work, the MARS-F code [37] is utilized to compute the linear stability for a series of equilibria with both pos-D and neg-D shapes. MARS-F solves the linearized, resistive MHD equations in toroidal geometry. The code solves the following set of equations in the plasma region as an eigenvalue problem, in a curvilinear coordinate system based on the equilibrium magnetic flux surfaces,

$$\gamma\boldsymbol{\xi} = \mathbf{v} \tag{1}$$

$$\rho\gamma\mathbf{v} = -\nabla p + \mathbf{j}\times\mathbf{B} + \mathbf{J}\times\mathbf{b} \tag{2}$$

$$\gamma\mathbf{b} = \nabla\times(\mathbf{v}\times\mathbf{B}) \tag{3}$$

$$\gamma p = -\mathbf{v}\cdot\nabla P - \Gamma P\nabla\cdot\mathbf{v} \tag{4}$$

where γ represents the (generally complex) eigenvalue of the mode. The equilibrium quantities are: the magnetic field $\mathbf{B}$, the plasma current $\mathbf{J}$, pressure P, and the plasma density ρ. The perturbed quantities $\boldsymbol{\xi}$, $\mathbf{v}$, p, $\mathbf{j}$, $\mathbf{b}$ represent the plasma displacement, perturbed velocity, plasma pressure, current density and magnetic field, respectively. $\Gamma = 5/3$ denotes the ratio of specific heats.

The vacuum region in MARS-F is modeled by solving equations $\nabla\times\mathbf{b} = 0$ and $\nabla\cdot\mathbf{b} = 0$, in the differential form, for the perturbed magnetic field $\mathbf{b}$. Since the Green's function approach is not utilized, the vacuum region is always finite in MARS-F (extending ten times the plasma minor radius). At the computational boundary, an ideal-wall boundary condition is imposed.

2.2. Series of semi-analytic equilibria with varying plasma boundary shape

To ensure that the equilibria are susceptible to infernal instabilities, NCS equilibria are generated with non-monotonic current density profiles for the purpose of systematic investigation, for plasmas with both pos-D and neg-D shapes. The radial profiles of the plasma equilibrium pressure P and the surface averaged toroidal current density $\langle J_\phi\rangle$ are analytically specified [38]

$$P(\psi_{\rm p}) = H\left(1-\frac{\psi_{\rm p}}{\psi_{\rm p}^{\rm ped}}\right)\left[1-\left(\frac{\psi_{\rm p}}{\psi_{\rm p}^{\rm ped}}\right)^{p_2}\right]^{p_3} \tag{5}$$

$$\langle J_\phi\rangle(\psi_{\rm p}) = \left(1-\psi_{\rm p}^{j_2}\right)^{j_3} + j_4\psi_{\rm p}^{j_5}(1-\psi_{\rm p})^{j_6} \tag{6}$$

where $\psi_{\rm p}$ is the normalized equilibrium poloidal magnetic flux, with $\psi_{\rm p} = 0$ and $\psi_{\rm p} = 1$ denoting the location at the magnetic axis and the plasma boundary, respectively. These radial

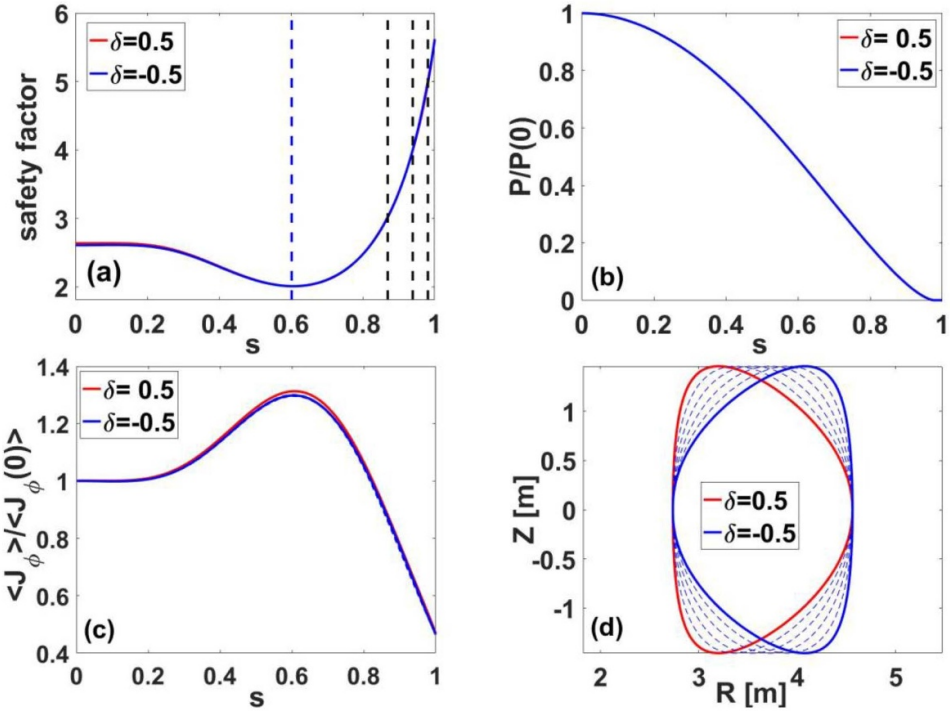

Figure 1. A series of equilibria with varying triangularity δ of the plasma boundary shape from $\delta = -0.5$ to 0.5 while fixing the safety factor profile and the $\beta_N(=2)$ value, showing (a)–(c) radial profiles of the safety factor, the equilibrium pressure, the surface-averaged toroidal current density, respectively, as well as (d) plasma boundary shapes. Here $s = (\psi_p)^{1/2}$ with ψ_p being the normalized equilibrium poloidal magnetic flux. Vertical dashed lines in (a) indicate the radial locations of the $n = 1$ rational surfaces. The vertical dashed line in blue shows the $q_{\min}$-location.

profiles are specified with free parameters p_k, $k = 2 \sim 3$ and j_k, $k = 2 \sim 6$. Other parameters are defined as $\psi_{\rm p}^{\rm ped} = 1 - \Delta$ with fixed $\Delta \equiv 0.05$ in this study. H is the Heaviside step function.

The plasma boundary shape is again analytically specified, in terms of the cylindrical coordinates R and Z and with a set of free parameters, k = 1~6,

$$R(\theta_{\rm U}) = 1 + b_1 \cos(\theta_{\rm U} + b_3 \sin(\theta_{\rm U})) \tag{7}$$

$$R(\theta_{\rm L}) = 1 + b_1 \cos(\theta_{\rm L} + b_4 \sin(\theta_{\rm L})) \tag{8}$$

$$Z(\theta) = b_1 b_2 \sin\theta - b_5 {\rm e}^{(-|\theta+\pi/2|/b_6)^{3/2}} \tag{9}$$

where θ is the poloidal angle. R and Z are normalized here by the major radius R_0 associated with the geometric center of the plasma column. In order to describe the plasma with the single-null-like boundary shape (associated with parameters b_5 and b_6), the poloidal angle is divided into the upper and lower halves denoted as $\theta_{\rm U}$ and $\theta_{\rm L}$. The parameter b_1 defines the inverse aspect ratio of the plasma, b_2 is the elongation, b_3 and b_4 determine the triangularity of the upper and lower plasma boundary shape, respectively. This work only focuses on the up-down symmetric shape. We thus have $\delta = b_3 = b_4$.

As an example, we show in figure 1 a series of equilibria in with $\delta = -0.5$, and with negative central magnetic field shear (the radial location of $q_{\min}$ is at $s_{\rm qmin} = 0.6$). The radial profile of the safety factor, the normalized equilibrium pressure and the normalized surface averaged toroidal current density are plotted in figures 1(a)–(c), respectively. These profiles are nearly identical for equilibria with varying plasma boundary shape shown in figure 1(d). All relevant parameters are summarized in table 1.

However, in order to clearly investigate the effect of the shape triangularity on the MHD mode stability, the whole radial profiles of the safety factor and normalized equilibrium pressure are fixed, as well as the value of $\beta_{\rm N}(=2)$, with varying the shape triangularity. We emphasize that the safety factor is an output (not input) of our equilibrium solver. To obtain the desired safety factor profile, we specify (and vary) the surface-averaged toroidal current density profile as the input

$$\left\langle \hat{J}_\phi \right\rangle = \langle J_\phi \rangle \times \left[j_1' + j_2' \left((\psi_p)^{1/2} - j_3' \right)^{j_4'} (\psi_p)^{j_5'/2} \right] + j_6' \psi_p \tag{10}$$

where j_k', $k = 1 \sim 6$ are free parameters which we (manually) tune. These tuned parameters, with varying triangularity between -0.4 and 0.5, are summarized in table 2.

The above analytic specification of the plasma boundary shape and the radial profiles for the plasma pressure and current density provides sufficient input data for numerical solution of the fixed-boundary Grad–Shafranov equation, resulting in self-consistent equilibria satisfying the MHD force balance. The Grad–Shafranov solver that we use is the CHEASE code [39]. We refer to these as semi-analytic equilibria, which give us the basis for perform stability analysis of the infernal-kink mode reported below while varying the plasma shape.

We emphasize that a (fixed) plasma boundary, not the external equilibrium coil currents, is specified as the input to

Table 1. Parameters p_k, j_k and b_k from equations (5)–(9), for specifying radial profiles of the equilibrium pressure, the surface-averaged toroidal current density and the plasma boundary shape, respectively, assuming the radial location of $q_{\min}$ at $s_{\mathrm{qmin}} = 0.6$ as shown by the red curve in figure 1.

quantities \ #	1	2	3	4	5	6
p_k		1	1.5			
j_k		1.8	2.9	65	2.22	4.85
b_k	0.25	1.6	—	—	0	1

Table 2. Parameters j_k' from equation (10), for specifying radial profiles of the surface-averaged toroidal current density assuming different values of the plasma boundary triangularity between −0.5 and 0.5. These values are obtained based on manual tuning to reach the desired safety factor profile.

$\delta = b_3 = b_4$	j_1'	j_2'	j_3'	j_4'	j_5'	j_6'
−0.5	1	0	0	0	0	0
−0.3	0.99	0.9	18	2.502	2.9	−0.033
−0.1	0.99	0.9	18	2.493	2.9	−0.022
0.1	0.99	0.9	16	2.48	2.9	0.035
0.3	1.04	0.9	16	2.48	2.9	0.035
0.5	1.0	0.9	−10	2.55	2.6	0.275

our equilibrium solver. The MARS-F stability calculations on the other hand assume a free-boundary condition and extend into the outer vacuum region.

3. Effect of triangularity on infernal-kink mode stability

We focus on the $n = 1$ mode stability. Because the instability that we consider here often contains external kink component, for which the wall stabilization plays a significant role, we will compare a free-boundary case without wall and a fixed-boundary case where an ideal conducting wall is placed at the plasma boundary. We start by reporting results without wall.

3.1. Effect of triangularity with fixed q-profile

For the equilibria (with the $q_{\min}$ radial location at $s_{\mathrm{qmin}} = 0.6$) shown in figure 1, the MARS-F computed growth rate of the $n = 1$ mode is reported in figure 2 while scanning δ from −0.5 to 0.5. As a significant observation, the growth rate is non-monotonic with increasing δ. In particular, a stable window opens for the pos-D shape, with the minimum growth rate (maximum damping rate) reached at $\delta \simeq 0.2$. Increasing triangularity towards neg-D shape or stronger pos-D shape destabilizes the mode. As will be elaborated later on, destabilization of the mode in plasmas with neg-D shape is primarily correlated to the averaged bad curvature.

The fact that $q_{\min}$ is close to 2 for our set of equilibria (figure 1(*a*)) suggests the onset of an infernal mode instability, which is indeed the case as confirmed by examining the computed mode eigenfunction. Figure 3 shows three representative

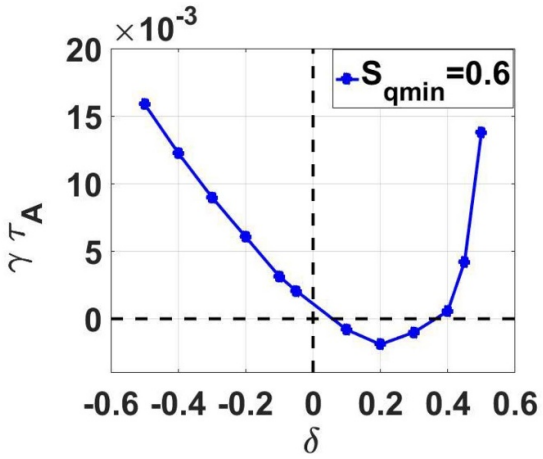

Figure 2. The MARS-F computed growth/damping rate of the $n = 1$ infernal-kink instability versus the plasma boundary triangularity δ, for the series of equilibria shown in figure 1 while fixing the radial location of $q_{\min}$ at $s_{\mathrm{qmin}} = 0.6$. The vertical dashed line indicates the value of triangularity $\delta = 0$.

examples with $\delta = -0.5$, -0.2 and 0.5, respectively, for the radial displacement of the plasma associated with the instability. It is evident that in all cases, the dominant (2/1) Fourier harmonic of the displacement peaks near the radial location of $q_{\min}$, at $s_{\mathrm{qmin}} = 0.6$. This is a typical infernal mode structure. We also note a rather global radial structure of instability which extends all the way to the plasma boundary. In particular, coupling to the external kink components (with finite radial displacement of the plasma boundary in figure 3(*c*)) is clearly identified for the equilibrium with strong pos-D shape. The eigenfunction shown in figure 3(*c*) is thus identified as an external kink instability.

3.2. Effect of radial location of q_{min}

The results reported so far have assumed a fixed safety factor profile while varying the plasma boundary shape. Since the infernal instability—both the mode location and growth rate—also depends on the radial location of $q_{\min}$, we vary this parameter as well. For this purpose, a set of new equilibria (figure 4) are generated following the same procedure as described in section 2.2. We vary in a relatively large range of [0.1, 0.6] while fixing the $q_{\min}$ value to be close to 2 (the global pressure parameter is also fixed at $\beta_{\mathrm{N}} = 2$ as before). Note that for each of the q-profile shown in figure 4, we also scan the triangularity parameter from −0.5 to 0.5, similar to what has been done in section 3.1. This yields a scan of the infernal-kink stability in the 2D parameter space of $(\delta, s_{\mathrm{qmin}})$. We also remark that the choice of the specific profiles here, especially for the case of $q_{\min} = 0.1$, is motivated by the earlier experimental results with positive triangularity and with a large central current hole [40–42].

Figure 5 reports the MARS-F computed mode growth/damping rate in the aforementioned 2D parameter space. In general, the growth rate of the infernal-kink is non-monotonic with increasing δ at a given s_{qmin}. A stable domain, enclosed

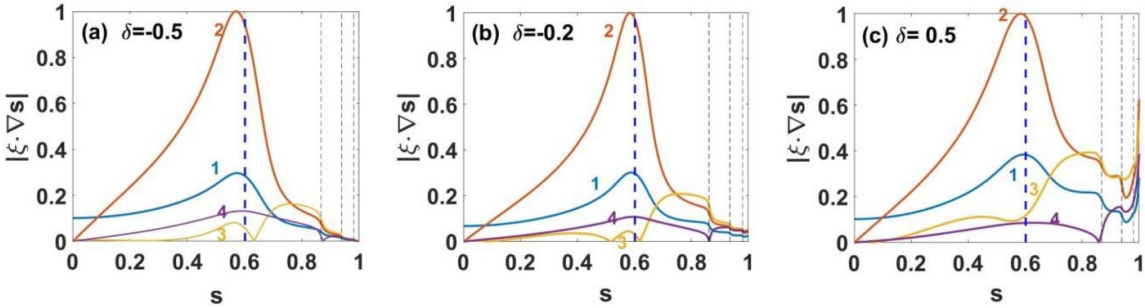

Figure 3. The computed mode eigenfunctions for the $n = 1$ (*a*) and (*b*) infernal and (*c*) external kink instabilities with $q_{\min}$-location of $s_{\mathrm{qmin}} = 0.6$, for three representative cases with the plasma boundary triangularity of (*a*) $\delta = -0.5$, (*b*) $\delta = -0.2$ and (*c*) $\delta = 0.5$, respectively. Plotted are radial profiles of the dominant poloidal Fourier harmonics ($m = 1$–4) for the radial displacement of the plasma due to the instability. Vertical dashed lines in black indicate the radial location of the $n = 1$ rational surfaces. Vertical dashed lines in blue show the $q_{\min}$-location ($s_{\mathrm{qmin}} = 0.6$). The normalized plasma pressure ($\beta_{\mathrm{N}} = 2$) is the same for all equilibria.

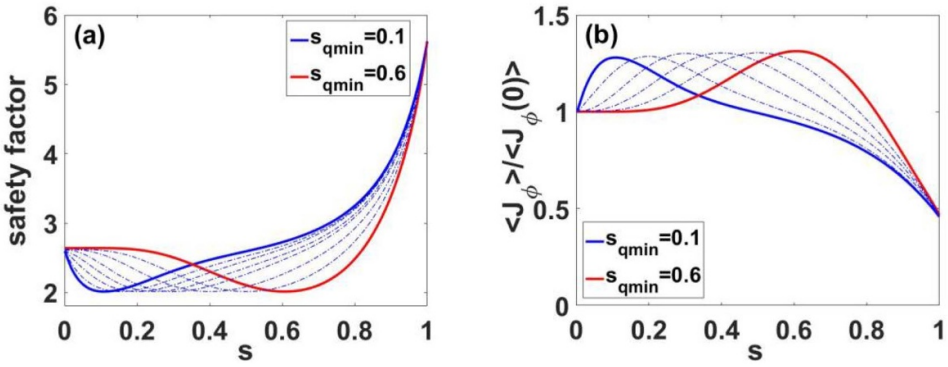

Figure 4. Assumed radial profiles of (*a*) the safety factor and (*b*) the corresponding surface-averaged toroidal current density, while varying the radial location (s_{qmin}) of $q_{\min}$ from 0.1 to 0.6 at fixed $q_{\min} = 2.01$. Each safety factor profile corresponds to a series of equilibria with the plasma boundary triangularity varying from -0.5 to 0.5 as shown in figure 1(*d*). The normalized plasma pressure is fixed at $\beta_{\mathrm{N}} = 2$ for all equilibria.

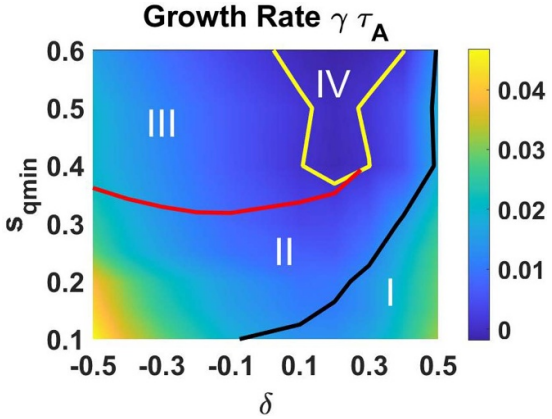

Figure 5. The MARS-F computed growth/damping rate of the $n = 1$ instability with vanishing wall, while varying both the plasma triangularity δ and the radial location (s_{qmin}) of $q_{\min}$. The safety factor profile is fixed as shown in figure 4. Four regions are identified: I—unstable external kink, II—unstable infernal-kink mode, III—unstable infernal mode, and IV—stable domain. The normalized plasma pressure is fixed at $\beta_{\mathrm{N}} = 2$ for all equilibria in this 2D parameter scan.

by the yellow curve in figure 5, appears in this 2D parameter space, when $q_{\min}$ is located sufficiently further away from the magnetic axis. Note that the stable window occurs only for pos-D shaped plasmas. The robustness of the infernal instability with minimal external kink contribution poses a MHD limitation to the neg-D scenario, if the latter is to be operated in the NCS regime.

We find that the robust instability at lower s_{qmin} values, occurring for all neg-D and pos-D equilibria considered here, tends to be more kink-like than infernal-like. These are

predominantly ideal external kink. This is illustrated in figure 6 for $s_{\rm qmin} = 0.1$. Note that the mode does not even peak at the $q_{\rm min}$ location, indicating a predominant kink drive by the plasma pressure.

Because of the variety of the mode eigenfunctions as we vary the equilibrium parameters, we delineate between distinct instabilities following a phenomenological approach. Specifically, we define two ratios among the amplitude of the poloidal Fourier harmonics of the radial displacement of the plasma as reported in figure 6

$$f_1 = \max|\xi_n^{nw}|_{m=2}/\max|\xi_n^{nw}|_{s=1,w/o\ m=2} \quad (11)$$

$$f_2 = \max|\xi_n^{nw}|_{m=2}/\max|\xi_n^{nw}|_{w/o\ m=2} \quad (12)$$

where f_1 is the ratio of the peak of the $m = 2$ radial displacement to the maximum amplitude of all the remaining poloidal harmonics at the plasma boundary $s = 1$ (excluding the $m = 2$ component), and f_2 is the ratio of the peak of the $m = 2$ radial displacement to the peak of all the remaining displacement harmonics (excluding the $m = 2$ component). We then refer to the instability as external kink if f_1 is below a critical value of $c_1 = 2$. This defines the region-I as denoted in figure 5. For the remaining unstable region, we apply the criterion $f_2 > c_2 = 3.27$ to identify the infernal mode instability (region-III in figure 5). Region-II corresponds to the coupled infernal-kink mode satisfying $f_2 < c_2$.

We note that the external kink instability indeed occurs as shown in figure 7, where we scan both the triangularity δ and $\beta_{\rm N}$. It is clear that with $s_{\rm qmin} = 0.1$ and at $\beta_{\rm N} = 2$, the ideal external kink becomes unstable as the plasma pressure exceeds the Troyon no-wall beta limit for the whole range of the δ values. For the case of $s_{\rm qmin} = 0.6$ (figure 7(b)), a stable window appears at $\beta_{\rm N} = 2$, consistent with that shown in figure 5.

In order to gain physics insight into the destabilization effect on the mode due to the neg-D shape, we consider two key equilibrium quantities associated with the shaping, that affect the low-n MHD instability. One is the Shafranov shift and the other the averaged magnetic curvature. For the infernal-kink type of mode which is partly driven by the plasma current and partly by the plasma pressure, and for equilibria with the same safety factor profile and the same global beta, the aforementioned two factors are the primary equilibrium quantities dictating the instability [43, 44].

Figure 8(a) reports the normalized Shafranov shift Δ/R_0 of the magnetic axis, while scanning both $s_{\rm qmin}$ and δ in the 2D parameter space. Here, $\Delta/R_0 = (R_{\rm axis} - R_0)/R_0$ with $R_0 = (R_{\rm max} + R_{\rm min})/2$. The Shafranov shift increases as the plasma boundary changes more towards the neg-D shape. Note again that this is primarily a shaping effect since we fix the global plasma pressure. Since Shafranov shift is typically stabilizing for the MHD modes [43], the trend shown in figure 8(a) does not explain the destabilization effect of the infernal-kink in neg-D plasmas.

On the other hand, in a tokamak geometry, the favorable average magnetic curvature effect is found to be stabilizing for the tearing and interchange modes [45]. The average curvature effect is often measured in terms of the Mercier Index D_R [44], which we evaluate at the $q_{\rm min}$ radial location for infernal mode. Because D_R is inversely proportional to the local magnetic shear $s_1 = (s/q)\,(\mathrm{d}q/\mathrm{d}s)$ [46], and hence approaches infinity at the $q_{\rm min}$ location for an NCS equilibrium, we examine instead the asymptotic quantity $s_1 D_R$ which remains finite at the magnetic shear reversal point.

This quantity is plotted in figure 8(b), again in the 2D parameter space of (δ, $s_{\rm qmin}$). Note that a negative value of D_R implies the stabilizing effect for the tearing and interchange modes in tokamaks. Figure 8(b) thus clearly quantifies the bad average curvature effect associated with the neg-D shape of the plasma, which is intuitively understandable since the equilibrium magnetic field lines tend to stay longer near the low-field side of the torus with a neg-D shape. This bad curvature effect, indicated by small negative or even positive values of $s_1 D_R$ in figure 8(b), destabilizes the infernal-kink mode as shown in figure 5.

We point out that the eventual mode stability reported in figure 5 results from the two competing effects as shown in figure 8, i.e. the stabilization due to the Shafranov shift and destabilization due to bad curvature, as the plasma shape changes towards more neg-D shapes [47, 48]. This competition is also likely the reason for the stable window for the infernal-kink instability shown in figure 5, as δ becomes slightly positive.

On the other hand, the stability window may not be solely determined by the aforementioned two competing effects. In particular, for plasmas with positive triangularity, strong curvature stabilization (with large negative D_R) occurs and at the same time certain Shafranov stabilization also occurs. Unstable modes are nevertheless still computed as shown in figure 5. This can be understood as a result of weakened Shafranov stabilization in positive triangularity plasmas. We also point out that both effects (Shafranov shift and toroidal curvature) are discussed here in a qualitative manner. The influences of the Shafranov stabilization and the bad-curvature destabilization are difficult to quantify for fully toroidal shaped plasmas.

Furthermore, we note that there are certainly other effects that also affect the MHD instability in general, such as the field line bending and the kink-drive associated with the plasma pressure or current gradients. In the context of the plasma shaping effects, i.e. the neg-D versus pos-D shapes, Shafranov shift and magnetic curvature appear to be the two most obvious physics/geometry factors, because these two quantities experience most changes as shown in figure 8, as we vary the plasma triangularity.

3.3. Infernal-kink stability with ideal wall

The presence of large external kink components in the computed mode, as shown in figures 3 and 6, complicates the stability analysis for these NCS plasmas with neg-D shape. In what follows, we try to eliminate these external kink components by placing an ideal wall at the plasma boundary, with the stability results reported in figures 9 and 10. We again identify three types of instability here. Defining a ratio similar to f_2 (but

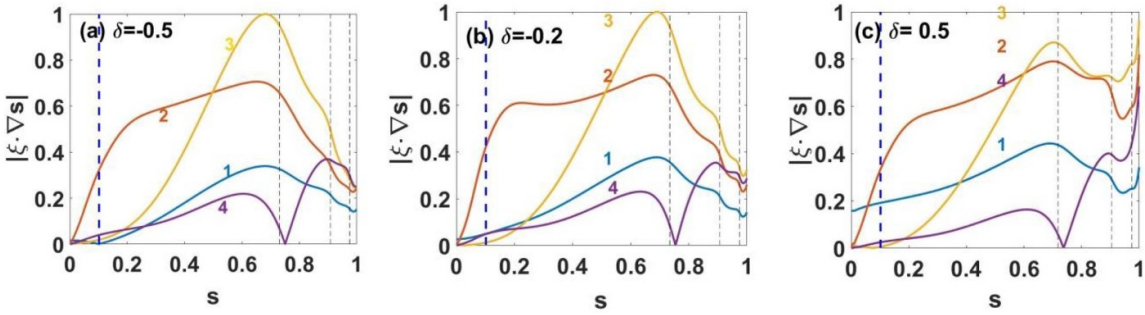

Figure 6. The computed mode eigenfunctions for the $n = 1$ no-wall (a), (b) infernal-kink and (c) external kink instabilities with $q_{\min}$-location of $s_{\text{qmin}} = 0.1$, for three representative examples with the plasma boundary triangularity of (a) $\delta = -0.5$, (b) $\delta = -0.2$ and (c) $\delta = 0.5$, respectively. Plotted are radial profiles of the dominant poloidal Fourier harmonics ($m = 1$–4) for the radial displacement of the plasma due to the instability. Vertical dashed lines in black indicate the radial location of the $n = 1$ rational surfaces. Vertical dashed lines in blue show the $q_{\min}$-location ($s_{\text{qmin}} = 0.1$). The normalized plasma pressure ($\beta_{\text{N}} = 2$) is the same for all equilibria.

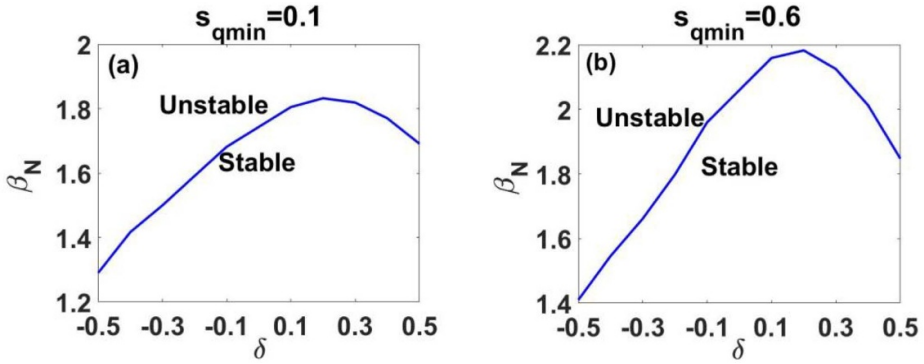

Figure 7. Stability boundary of the $n = 1$ infernal-kink instability, computed in the 2D parameter space of (δ, β_{N}) while fixing the $q_{\min}$-location at (a) $s_{\text{qmin}} = 0.1$, and (b) $s_{\text{qmin}} = 0.6$, respectively.

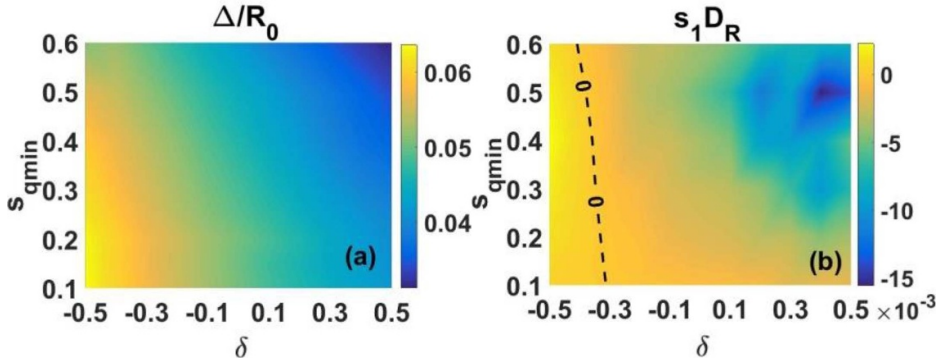

Figure 8. (a) Shafranov shift Δ of the equilibrium magnetic axis, normalized by the major radius R_0, and (b) the asymptotic quantity $s_1 D_R$ evaluated at the radial location (s_{qmin}) of $q_{\min}$, with s_1 and D_R being the magnetic shear and the tearing index, respectively. Varied parameters are both the plasma boundary triangularity δ and the radial location (s_{qmin}) of $q_{\min}$. Here, the $n = 1$ no-wall infernal-kink instability is considered.

for the radial displacement in the presence of an ideal wall)

$$f_3 = \max\left|\xi_n^{iw}\right|_{m=2} / \max\left|\xi_n^{iw}\right|_{w/o\ m=2} \tag{13}$$

We refer to the instability as global internal kink if $f_3 < c_3 = 2$. We then apply the same criterion c_2 (as from section 3.2) to distinguish between the infernal ($f_3 > c_2$) and infernal-kink ($c_3 < f_3 < c_2$) instabilities.

Figure 9 plots the MARS-F computed mode growth/damping rate in the 2D parameter space (δ, s_{qmin}), for the same sets of equilibria as in figure 5. It is evident that the ideal wall stabilization expands the stable window in the aforementioned parameter space. In particular, the infernal-kink instability disappears in all plasmas with the pos-D shape. The infernal mode is also stable for all pos-D configurations. The marginal stable curve from figure 9 is not very sensitive to the radial location of $q_{\min}$, indicating that the plasma boundary shape

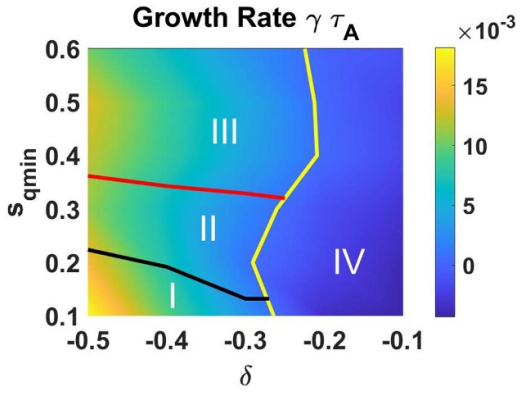

Figure 9. The MARS-F computed growth rate of the $n = 1$ instability with an ideal wall, while varying both the plasma triangularity δ and the radial location ($s_{\rm qmin}$) of $q_{\rm min}$. The safety factor profile is fixed as shown in figure 4. Four regions are identified, corresponding to I—global internal kink instability, II–infernal-kink instability, III–infernal instability, and IV—stable domain. The normalized plasma pressure is fixed at $\beta_{\rm N} = 2$ for all equilibria in this 2D parameter scan.

(triangularity) is the main factor determining the infernal-kink stability here. Coming back to the physics discussion presented in section 3.2, we conclude that, in strongly shaped neg-D plasmas with NCS, the bad curvature destabilization overcomes the stabilizing influence by the Shafranov shift, with a net effect which is still destabilizing for the infernal-type of mode.

The infernal nature of the instability becomes more pronounced with the ideal-wall stabilization, as shown by the mode eigenfunction from figure 10. Here, we choose to compare three cases with moderate neg-D triangularity ($\delta = -0.3$), but with different radial locations of $q_{\rm min}$, i.e. $s_{\rm qmin} = 0.1$, 0.3 and 0.6. When $q_{\rm min}$ is located too close to the magnetic axis, the global kink coupling still occurs (figure 10(*a*)), but the largest Fourier harmonic already shifts to the $m/n = 2/1$ infernal component which peaks near the $q_{\rm min}$ location. As $q_{\rm min}$ shifts away from the magnetic axis (figures 10(*b*) and (*c*)), the infernal component becomes dominant which may prevent the ITB formation. Note also that in all cases, vanishing plasma displacement occurs at the plasma boundary due to the ideal-wall boundary condition.

3.4. Further identification of the nature of instability

The presence of the kink component discussed so far, as well as the plasma shaping factors (toroidicity, elongation, triangularity, etc.) induced mode coupling, renders characterization of the infernal instability challenging in neg-D shaped NCS plasmas. In what follows, we further identify the mode, by systematically investigating the influence of the value and plasma pressure on the mode growth rate.

We have so far fixed the plasma pressure (at $\beta_N = 2$) and the $q_{\rm min}$ value (close to 2) while studying the shaping effect (the plasma boundary triangularity). On the other hand, it is known that both proximity of $q_{\rm min}$ to a rational number and the plasma pressure drive the infernal instability [47]. We will therefore vary these two parameters while fixing the triangularity. We choose two extreme cases for the latter ($\delta = -0.5$ and 0.5).

Figure 11 reports several representative results. Note that we also show two cases with different radial locations of $q_{\rm min}$, with $s_{\rm qmin} = 0.1$ and $s_{\rm qmin} = 0.6$, respectively. Previous results (figures 6 and 10) already indicate somewhat different nature of instability between these two cases. Several interesting observations can be made from figure 11.

First, for the equilibria with pos-D shape ($\delta = 0.5$, figurse 11(*a*) and (*d*)), the computed mode growth rate peaks near, but generally not exactly at, the integer value of $q_{\rm min} = 2$ (for the $n = 1$ instability). We attribute the slight shift of the peaks from, shown in figures 11(*a*) and (*d*), by the poloidal mode coupling effect as the main reason. Indeed, as shown in figures 6 and 10, the relative amplitudes of the sideband (with respect to $m = 2$) poloidal harmonics are not small. We emphasize, however, that the parabolic-like behavior of the mode growth rate versus $q_{\rm min}$ cannot be used as the sufficient condition for identifying the infernal mode. Indeed, the mode eigenfunctions shown in figures 6(*c*) and 10(*a*) that correspond to figure 11(*a*), do not show the infernal component as the dominant portion of the mode structure.

Next, we consider cases with the neg-D shape (figures 11(*b*) and (*e*)). Here, the mode stability behavior (versus $q_{\rm min}$) is very different between the two cases of $s_{\rm qmin} = 0.1$ and 0.6. We identify the former as a global internal kink instability. Note that this is not an external kink-peeling mode, since the mode remains unstable even with an ideal wall placed at the plasma boundary (figure 11(*c*)). The similar monotonic dependence of the growth rate on $q_{\rm min}$ shows that the instability is not an infernal mode even with wall stabilization.

Lastly, we turn to the influence of the plasma pressure on the mode stability. The pressure drive on the infernal-kink mode is evident from figures 11(*b*) and (*c*)) with neg-D plasma shape. Note that the dominant mode becomes $m = 3$ here, because $q_{\rm min}$ exceeds 2 and the q-profile has low magnetic shear at $q = m/n = 3/1$ as well as near $q_{\rm min}$. The pressure drive on the infernal mode (affected by the poloidal mode coupling mentioned earlier), reported in figures 11(*e*) and (*f*)) for neg-D plasmas, also follows theoretical expectation, i.e. the mode becomes more unstable at higher equilibrium pressure. For the pos-D cases (figures 11(*a*) and (*d*)), higher equilibrium pressure enhances the peak value of the growth rate following each curve. Because the peak location sensitively varies with $\beta_{\rm N}$ in these cases, the pressure drive is not uniform for all curves.

Figure 12 compares the computed eigenfunctions for the $n = 1$ infernal-kink between the pos-D and neg-D equilibria (at fixed pressure $\beta_{\rm N} = 2$ and $q_{\rm min} = 2.01$). The dominant mode changes from $m = 2$ (figure 12(*a*)) to $m = 3$ (figure 12(*b*)), when the magnetic shear reversal layer moves from the middle of the plasma column (figure 12(*a*)) towards the magnetic axis (figure 12(*b*)). In this case, the plasma shaping weakly affects the mode structure. (The ideal-wall boundary condition enforces vanishing displacement at the plasma boundary

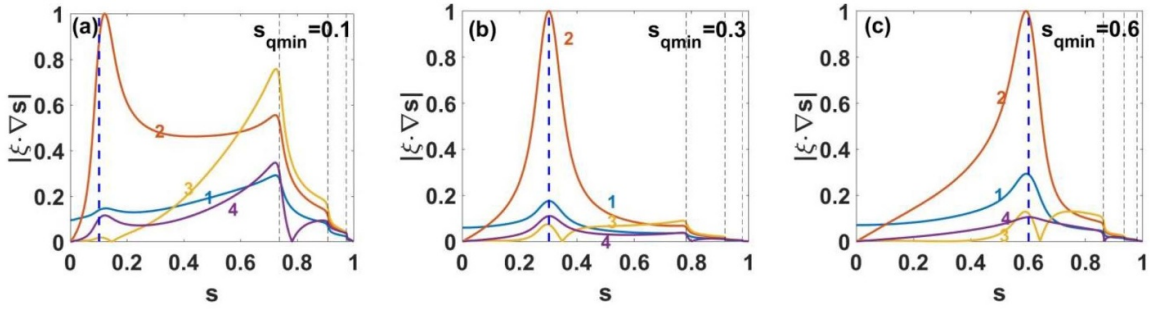

Figure 10. The computed mode eigenfunctions of the $n = 1$ (*a*) global internal kink instability, (*b*) infernal and (*c*) infernal-kink instability with an ideal wall right at the plasma boundary, for three representative examples with the radial location of $q_{\rm min}$ at (*a*) $s_{\rm qmin} = 0.1$, (*b*) $s_{\rm qmin} = 0.3$ and (*c*) $s_{\rm qmin} = 0.6$, respectively. The plasma boundary triangularity is fixed at $\delta = -0.3$. Plotted are radial profiles of the dominant poloidal Fourier harmonics ($m = 1$–4) for the radial displacement of the plasma due to the instability. Vertical dashed lines in black indicate the radial location of the $n = 1$ rational surfaces. Vertical dashed lines in blue show the $q_{\rm min}$-location. The normalized plasma pressure ($\beta_{\rm N} = 2$) is the same for all equilibria.

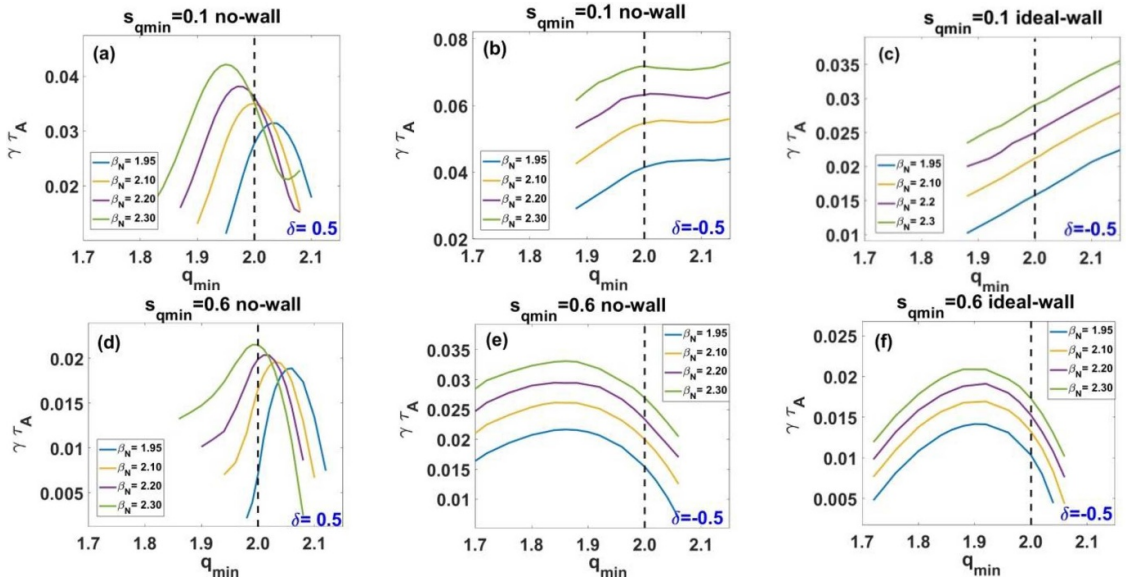

Figure 11. The MARS-F computed growth rate of the $n = 1$ infernal-kink instability versus the q-value of $q_{\rm min}$ while varying the plasma pressure $\beta_{\rm N}$, for (*a*), (*d*) the pos-D shapes ($\delta = 0.5$) and (*b*), (*c*), (*e*), (*f*) the neg-D shapes ($\delta = -0.5$). In the upper and bottom panels plot the radial location of $q_{\rm min}$ at $s_{\rm qmin} = 0.1$ and $s_{\rm qmin} = 0.6$, respectively. Two wall conditions are considered, including (*a*), (*b*), (*d*), (*e*) the no-wall condition and (*c*), (*f*) the ideal-wall condition. Here the black vertical lines denote the q-value of $q_{\rm min}$ (=2).

as already noted earlier.) On the contrary, global kinks, with strong poloidal coupling, appear when $q_{\rm min}$ is close to the magnetic axis (figure 12(*b*)). The plasma triangularity also exerts a stronger influence on the mode eigenfunction in this case.

Our study has so far been focusing on the $n = 1$ instability, which is most macroscopic in terms of the toroidal wavelength and is typically the most dangerous one in tokamak plasmas. On the other hand, it is well-known that high-n infernal instability also occurs, and the mode growth rate exhibits oscillations with increasing toroidal mode number [28]. Such oscillation behaviors are also recovered by MARS-F, as long as the infernal mode is the dominant component of the computed eigenfunction. Computations assuming different $q_{\rm min}$-values have also been performed, with one example reported in figure 13(*a*) where we choose an equilibrium with $s_{\rm qmin} =$ 0.6. We find that this oscillating behavior is somewhat sensitive to the choice of the $q_{\rm min}$value ($q_{\rm min} = 2.2$ in the example shown). This is not surprising given the fact that the oscillation is mainly dictated by proximity of $q_{\rm min}$ to rational numbers *m/n* for the infernal mode instability. The latter is illustrated by figure 13(*b*), where we plot the minimum distance (among all poloidal harmony numbers) $\mathrm{f}(n) = \min|q_{\rm min} - m/n|$ of $q_{\rm min}$ to rational numbers *m/n*, while scanning n at fixed $q_{\rm min}$.

We make a remark on the choice of the high value of $\beta_{\rm N} = 3.54$ in figure 13. High equilibrium pressure is required to drive higher-n infernal mode unstable. We thus choose a high-$\beta_{\rm N}$ equilibrium to ensure that unstable modes are still computed as we scan n. Such a high-$\beta_{\rm N}$ plasma may not be easily achievable though in experiments.

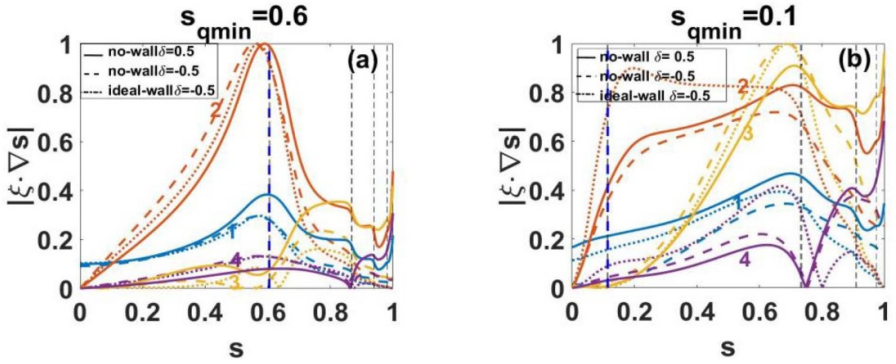

Figure 12. The computed mode eigenfunctions of the $n = 1$ instabilities, for two series of representative examples with the radial location of $q_{\min}$ at (*a*) $s_{\rm qmin} = 0.6$ and (*b*) $s_{\rm qmin} = 0.1$, respectively. Plotted are radial profiles of the dominant poloidal Fourier harmonics ($m = 1$–4) for the radial displacement of the plasma due to the instability. In plot (*a*) with, three representative examples are considered where the solid and dashed curves denote the computed eigenfunctions of the no-wall external kink and infernal instabilities with $\delta = 0.5$ and, respectively. The dotted curves denote the infernal instability with an ideal wall right at the plasma boundary with $\delta = -0.5$. In plot (b) with $q_{\min} = 0.1$, the solid and dashed curves denote the no-wall external kink and infernal-kink instabilities with $\delta = 0.5$ and $\delta = -0.5$, respectively. The dotted curves denote the global internal kink with an ideal wall right at the plasma boundary and the plasma boundary with $\delta = -0.5$. Vertical dashed lines in black indicate the radial location of the $n = 1$ rational surfaces. Vertical dashed lines in blue show the $q_{\min}$-location. The normalized plasma pressure ($\beta_{\rm N} = 2$) is the same for all equilibria.

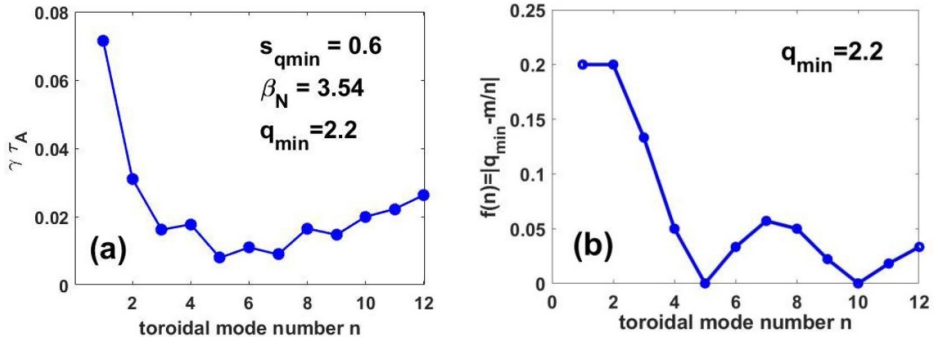

Figure 13. (*a*) The MARS-F computed growth rate of the infernal-kink mode versus the toroidal mode number n, with the plasma pressure fixed at $\beta_{\rm N} = 3.54$ and the radial location of $q_{\min} = 2.2$ at $s_{\rm qmin} = 0.6$. (*b*) The analytic dependence of the f(n) factor on the toroidal mode number n, with $q_{\min} = 2.2$. The plasma boundary triangularity is fixed at $\delta = -0.5$.

4. Conclusion and discussion

We have performed numerical investigation into the stability of the $n = 1$ ideal infernal-kink instability in neg-D plasmas with NCS for the equilibrium safety factor. The latter is motivated by the desire to form the ITB in the neg-D configuration, which is known to have difficulty to form the ETB. We also contrast the MHD stability results with that from the pos-D configuration, with otherwise similar equilibrium profiles (the plasma pressure, toroidal current density as well as the safety factor). All stability computations are carried out utilizing the MARS-F code, based on a series of semi-analytically designed equilibria with varying plasma boundary shape.

As a key conclusion, we find that infernal-kink mode is generally more unstable in neg-D plasmas as compared to the pos-D counterpart. This poses certain MHD limitations on achieving stable operational regime with ITB and with the neg-D concept. Based on our numerical findings, we propose a recipe for resolving this issue, by (i) forming the ITB not too close to the magnetic axis in neg-D plasmas to avoid strong kink-drive, and (ii) by allowing $q_{\min}$ further away from rational numbers (integer numbers for the $n = 1$ instability) to avoid the infernal drive.

For comparison, we find that the infernal-kink mode is more stable in pos-D plasmas with the same safety factor profile and the same $\beta_{\rm N}$ value. In fact, a stable window opens up near $\delta \sim 0.2$ for the $n = 1$ infernal mode (with sufficient large $s_{\rm qmin}$ and without wall stabilization), as we scan triangularity of the plasma boundary shape. Imposing an ideal-wall boundary condition suppresses the external kink drive, leading to wider stable windows extending to the neg-D regime ($\delta > -0.25$).

Physics-wise, we find that the more unstable behavior of the infernal-kink mode with the neg-D configuration is mainly due to less favorable (or even unfavorable) average magnetic curvature near the $q_{\min}$ location, as compared to the pos-D counterpart. The larger Shafranov shift associated with the neg-D shape helps the mode stabilization, but is not sufficient to overcome the destabilizing effect due to bad curvature. On the other hand, the aforementioned two competing effects can

be employed to explain the non-monotonic dependence of the computed mode growth rate versus δ and the appearance of the stable window at intermediate (positive) delta values. As another interesting physics point, we identify a strong poloidal mode coupling due to plasma shaping (toroidicity, elongation, triangularity, etc), which helps explain the slight shift (with respect to that predicted by the analytic theory) of the peak location of the mode growth versus $q_{\min}$.

We remark that this study focuses on ideal MHD stability analysis. The plasma equilibrium flow is also neglected. The plasma toroidal flow, as well as effects beyond ideal MHD, may also affect the infernal-kink stability in the neg-D configuration, which is the subject of future detailed studies. We point out though that for an ideally unstable MHD mode, the non-ideal effects (finite plasma resistivity, drift kinetic effects, etc) typically do not produce qualitative changes to the mode stability. The plasma toroidal flow should also have limited effects on the infernal-like instability which is largely internal to the plasma and relatively local in terms of the plasma displacement induced by the mode. This is unlike the resistive wall mode (essentially an external kink instability) which is subject to flow damping associated with various Landau resonance physics. Furthermore, stabilizing effect of trapped thermal ions on infernal modes has been identified in the context of the edge-localized infernal mode [19], provided that the mode is not too unstable (to allow sufficient kinetic resonance damping). In realistic conditions kinetic effects from high-energy particles and thermal trapped ions can stabilize the core Mercier modes [11]. Energetic particles may also affect the infernal mode stability via conservation of the third adiabatic invariant. Drift kinetic resonance effects of EPs may play certain roles as well but this remains to be carefully studied.

Acknowledgments

This work is funded by National Key R&D Program of China under Contract No. 2022YFE03060002 and 2024YFE03010000, by National Natural Science Foundation of China (NSFC) [Grant Nos. 12075053, 11505021 and 11975068], and by the Central Universities [Grant No. 232025G-10]. The work was also supported by the U.S. DoE Office of Science under Contract No. DE-FG02–95ER54309. This report was prepared as an account of work sponsored by an agency of the United States Government. Neither the United States Government nor any agency thereof, nor any of their employees, makes any warranty, express or implied, or assumes any legal liability or responsibility for the accuracy, completeness, or usefulness of any information, apparatus, product, or process disclosed, or represents that its use would not infringe privately owned rights. Reference herein to any specific commercial product, process, or service by trade name, trademark, manufacturer, or otherwise, does not necessarily constitute or imply its endorsement, recommendation, or favoring by the United States Government or any agency thereof. The views and opinions of authors expressed herein do not necessarily state or reflect those of the United States Government or any agency thereof.

ORCID iDs

Y.Q. Liu https://orcid.org/0000-0002-8192-8411
J.W. Li https://orcid.org/0000-0002-9216-105X
Y. Liang https://orcid.org/0000-0002-9483-6911
F.C. Zhong https://orcid.org/0000-0002-4038-4040

References

[1] Wolf R.C. *et al* 2002 *Plasma Phys. Control. Fusion* **45** R1
[2] Koide Y. *et al* 1994 *Phys. Rev. Lett.* **72** 3662
[3] Takenaga H. *et al* (the JT-60 Team) 2003 *Nucl. Fusion* **43** 1235
[4] Wagner F. *et al* 1982 *Phys. Rev. Lett.* **49** 1408
[5] Loarte A. *et al* 2007 *Phys. Scr.* **2007** 222
[6] Gunn J.P. *et al* 2017 *Nucl. Fusion* **57** 046025
[7] Kikuchi M. *et al* 2014 *12th Asia Pacific Physics Conf. (Makuhari, Japan, 14-19 July 2013)* **1** 015014
[8] Thome K.E. *et al* 2024 *Plasma Phys. Control. Fusion* **66** 105018
[9] Paz-Soldan C. *et al* 2024 *Nucl. Fusion* **64** 094002
[10] Boyes W., Turco F., Hanson J., Marinoni A., Turnbull A., Austin M. and Navratil G. 2023 *Nucl. Fusion* **63** 086007
[11] Medvedev S.Y. *et al* 2015 *Nucl. Fusion* **55** 063013
[12] Kikuchi M. *et al* 2019 *Nucl. Fusion* **59** 056017
[13] Pochelon A. *et al* 1999 **39** 1807
[14] Coda S. *et al* 2022 *Plasma Phys. Control. Fusion* **64** 014004
[15] Camenen Y., Pochelon A., Behn R., Bottino A., Bortolon A., Coda S., Karpushov A., Sauter O. and Zhuang G. (the TCV Team) 2007 *Nucl. Fusion* **47** 510
[16] Zheng L., Kotschenreuther M.T. and Waelbroeck F.L. 2021 *Nucl. Fusion* **61** 116014
[17] Yang X., Liu Y., Xu W., He Y. and Xia G. 2023 *Nucl. Fusion* **63** 066001
[18] Ren J., Liu Y., Liu Y., Medvedev S.Y., Wang Z. and Xia G. 2016 *Plasma Phys. Control. Fusion* **58** 115009
[19] Dong G.Q., Liu Y.Q., Wang S., Zhang N., Yu D.L., Liu Y. and Wang Z.R. 2017 *Phys. Plasmas* **24** 112510
[20] Nelson A.O., Paz-Soldan C. and Saarelma S. 2022 *Nucl. Fusion* **62** 096020
[21] Yu G. *et al* 2023 *Phys. Plasmas* **30** 062505
[22] Connor J.W., Fukuda T., Garbet X., Gormezano C., Mukhovatov V. and Wakatani M. (the ITB Database Group, the ITPA Topical Group on Transport and Internal Barrier Physics) 2004 *Nucl. Fusion* **44** R1
[23] Lao L.L. *et al* 1996 *Phys. Plasmas* **3** 1951–8
[24] Wade M.R. *et al* 2001 *Phys. Plasmas* **8** 2208–16
[25] Leboeuf J.N., Lynch V.E. and Carreras B.A. 2001 *Phys. Plasmas* **8** 3358–66
[26] Rodríguez E. *et al* 2023 *J. Plasma Phys.* **89** 05890211
[27] Masamoto Y., AIBA N. and Furukawa M. 2022 *Plasma Fusion Res.* **17** 2403038
[28] Manickam J., Pomphrey N. and Todd A.M.M. 1987 *Nucl. Fusion* **27** 1461
[29] Sato M., Todo Y., Aiba N. and Takechi M. 2024 *Nucl. Fusion* **64** 076021
[30] Graves J.P., Coste-Sarguet M. and Wahlberg C. 2022 *Plasma Phys. Control. Fusion* **64** 014001
[31] Brunetti D., Ham C.J., Graves J.P., Wahlberg C. and Cooper W.A. 2020 *Plasma Phys. Control. Fusion* **62** 115005
[32] Ishida Y., Ishizawa A., Imadera K., Kishimoto Y. and Nakamura Y. 2020 *Phys. Plasmas* **27** 092302
[33] Kleiner A., Graves J.P., Brunetti D., Cooper W.A., Halpern F.D., Luciani J.-F. and Lütjens H. 2016 *Nucl. Fusion* **56** 092007
[34] Wahlberg C. and Graves J.P. 2007 *Phys. Plasmas* **14** 110703

[35] Chapman I.T., Hua M.D., Pinches S.D., Akers R.J., Field A.R., Graves J.P., Hastie R.J. and Michael C.A. (the MAST Team) 2010 *Nucl. Fusion* **50** 045007
[36] Wei D. *et al* 2014 *Nucl. Fusion* **54** 013010
[37] Liu Y.Q., Bondeson A., Fransson C.M., Lennartson B. and Breitholtz C. 2000 *Phys. Plasmas* **7** 3681–90
[38] Liu Y.Q., Lao L., Li L. and Turnbull A.D. 2020 *Plasma Phys. Control. Fusion* **62** 045001
[39] Lütjens H., Bondeson A. and Sauter O. 1996 *Comput. Phys. Commun.* **97** 219
[40] Rice B.W. *et al* 1996 *Plasma Phys. Control. Fusion* **38** 869–81
[41] Hawkes N.C. *et al* 2001 *Phys. Rev. Lett.* **87** 115001
[42] Fujita T. *et al* 2001 *Phys. Rev. Lett.* **87** 245001
[43] Greene J.M. and Chance M.S. 1981 *Nucl. Fusion* **21** 453
[44] Glasser A.H., Greene J.M. and Johnson J.L. 1975 *Phys. Fluids* **18** 875–88
[45] Glasser A.H., Greene J.M. and Johnson J.L. 1976 *Phys. Fluids* **19** 567–74
[46] Hastie R. and Hender T.C. 1988 *Nucl. Fusion* **28** 585
[47] Kotschenreuther M., Hazeltine R.D. and Morrison P.J. 1985 *Phys. Fluids* **28** 294–302
[48] Shafranov V.D. 1968 *Nucl. Fusion* **8** 253